Single ionization of helium by fast proton impact in different kinematical regimes

O. Chuluunbaatar,[1,2] K. A. Kouzakov,[3] S. A. Zaytsev,[4] A. S. Zaytsev,[4] V. L. Shablov,[5] Yu. V. Popov,[6,1] H. Gassert,[7] M. Waitz,[7] H.-K. Kim,[7] T. Bauer,[7] A. Laucke,[7] Ch. Müller,[7] J. Voigtsberger,[7] M. Weller,[7] J. Rist,[7] K. Pahl,[7] M. Honig,[7] M. Pitzer,[7] S. Zeller,[7] T. Jahnke,[7] L. Ph. H. Schmidt,[7] H. Schmidt-Böcking,[7] R. Dörner,[7] and M. S. Schöffler[7,*]

[1]*Joint Institute for Nuclear Research, Dubna, Moscow Region 141980, Russia*

[2]*Institute of Mathematics, National University of Mongolia, UlaanBaatar 14201, Mongolia*

[3]*Faculty of Physics, Lomonosov Moscow State University, Moscow 119991, Russia*

[4]*School of Fundamental and Computer Sciences, Pacific National University, Khabarovsk 680035, Russia*

[5]*Obninsk Institute for Nuclear Power Engineering of the National Research Nuclear University MEPhI, Kaluga Region 249040, Russia*

[6]*Skobeltsyn Institute of Nuclear Physics, Lomonosov Moscow State University, Moscow 119991, Russia*

[7]*Institut für Kernphysik, Universität Frankfurt, 60438 Frankfurt, Germany*

(Received 16 March 2019; revised manuscript received 30 April 2019; published 25 June 2019)

We present ultrahigh-resolution data on fully differential cross sections for single ionization of helium induced by 1 MeV proton impact. In the present work we explore a different regime of kinematic conditions in terms of momentum transfer and electron energies than previously published data. These data are compared with different theoretical calculations. Reasonable agreement between the first Born approximation and experiment is obtained in the kinematic regime close to the Bethe ridge. Far from this region the calculated binary peak is shifted with respect to experiment. In order to resolve this problem, we analyze several theoretical mechanisms beyond the customary first Born approximation theory. These mechanisms include the 3C model (three Coulomb functions), effective charges, off-shell pair T matrices instead of pair potentials, and semiclassical postcollision interaction. We find that a combination of the 3C model with a semiclassical postcollision interaction effect may explain the observed discrepancy.

DOI: 10.1103/PhysRevA.99.062711

I. INTRODUCTION

The study of atomic ionization by fast ions is of fundamental importance for atomic collision physics and for the physics of penetration of swift ions through matter, including applications in radiation material science [1] and ion therapy [2,3]. One of the most powerful tools in this field of research is the cold target recoil ion momentum spectroscopy (COLTRIMS) [4–9]. This technique is capable of determining the three-dimensional angular distribution of electrons emitted at given values of energy and momentum transfer with unprecedented precision [10,11]. This is achieved by the coincident measurement of electron and ion momentum vectors. Such fully differential cross sections (FDCSs) provide very detailed information about the ionization process and thus greatly stimulate the development of the relevant theoretical methods and approaches, ranging from the customary perturbation treatments, such as the first and second Born approximations, to the well-known continuum distorted-wave–eikonal initial-state (CDW-EIS) model [12,13] and the time-dependent and convergent close-coupling calculations (TDCCs [14] and CCCs [15], respectively).

In our previous study [16], we reported high-resolution data for the emission of electrons with energy $E_e = 6.5 \pm 3.5$ eV in 1-MeV proton-helium collisions at momentum transfer $q = 0.75 \pm 0.25$ a.u. For comparison with theory, we employed both the usual first Born approximation (FBA) with respect to the proton-helium interaction, where the incident and scattered proton states are treated as plane waves, and the eikonal wave Born approximation that accounts for the eikonal distortion effects in the final channel. The data exhibited a well-pronounced nodal structure, which is in agreement with FBA predictions. At the same time, some discrepancy between FBA and experiment was found in the scattering plane: the binary and recoil peaks appear to be shifted towards smaller emission angles compared to the FBA calculations. In the recent work [17] we already used the second Born approximation (SBA) and the 3C (or BBK) model [18], which takes into account interactions between all three final fragments. The theoretical calculations have been compared with experiment in coplanar geometry. In order to explain the ratio of recoil- to binary-peak intensity, it has been shown that it is also necessary accounting for the strong effect of electron-electron correlations in the ground state of the He atom [17]. The 3C model reasonably agrees with experiment in the recoil peak, but a discrepancy of a few degrees with experiment still remains in the case of the binary peak. This means that further investigation of the origin of the disagreement between theory and experiment is necessary.

There are two main, seemingly different approaches usually employed in the theoretical treatment of reactions involving fast protons. In the one approach, the time-dependent Schrödinger equation (TDSE) is considered, where the incident proton acts as a classical particle, i.e., a moving point source of the electric field. In the other approach, using the time-independent Schrödinger equation (TISE), all three

*schoeffler@atom.uni-frankfurt.de

particles are treated quantum mechanically. In both cases one often uses the CDW-EIS model (see, for instance, the useful review articles [19,20]). It is worth mentioning that the 3C function can also be considered within the CDW approximation. Another frequently employed method for calculating the final state of three charged particles is the CCC theory. There are a great number of publications devoted to this method, so we limit ourselves to mentioning only the basic work [21]. In the framework of the CCC theory, the final-state wave function is approximated by a superposition of basis wave functions of a discrete spectrum with positive energies constructed in a certain way. Since this approximation is not used in this study, we will not dwell on it in detail.

Let us discuss those works in which, to our knowledge, the shift of a binary peak was inspected. In addition to protons, we also discuss antiproton projectiles. In the usual version of FBA (i.e., where both the incident and scattered projectile states are described with plane waves), the binary and recoil peaks are back-to-back and rotationally symmetric around the direction of the momentum transfer $\vec{q} = \vec{p}_i - \vec{p}_s$, where $\vec{p}_{i(s)}$ is the incident (scattered) projectile momentum. In other words, in this version the momentum-transfer vector is the only "external" vector that defines the symmetry axis for the distribution of the ejected-electron momentum $\vec{k}_e$. When going beyond the FBA theory, for example, when using distorted waves, the proton velocity vector $\vec{v}_p$ also comes into play, and the peaks can shift. In the case of protons, one might expect the peaks to be shifted towards the z axis (the incoming proton velocity vector), since the electron is attracted to the proton. In the case of an antiproton, the shift should occur in the opposite direction. This is indeed the case, regardless of the theories used: here are just a few works from the long list [17,22–25].

However, close inspection shows interesting features. In Ref. [17], the contributions from the final-state proton-electron (*pe*) and proton-nucleus (*pN*) interactions in the 3C model were studied separately. It was found that the *pN* interaction shifts the binary peak of the electron distribution to smaller angles between the projectile proton and the electron, whereas the *pe* interaction, on the contrary, shifts the peak away from the proton. Their joint action "attracts" the electron to the proton (a similar effect was observed in Ref. [26]). At the same time, in the work [25], where the scattering of an antiproton on atomic hydrogen was investigated in the framework of the TDCC theory, the $p^- N$ interaction was found to have practically no effect on the position of the binary peak. We note that this interaction is introduced into the theory by a standard, but *ad hoc*, method, and the energy of the antiproton was relatively small there. Thus, the problem of the shift of the peak and the magnitude of this shift at various kinematic parameters and, depending on the approximation used, remains a very interesting issue both for theory and for experiment.

In the present case of single ionization of helium, one may assume that the incident energy of 1 MeV and higher should be enough for the first-order theories to be valid. Most of the calculations have been done for the kinematic regime of small momentum transfer (0.75 a.u.) and low ejected-electron energy (6 eV). Even for such kinematics the calculations within two distinct approaches of, respectively, Refs. [17] and [22] give practically the same shift of the binary peak with respect to the FBA position. This shift turns out to be too small for explaining the experiment. In this connection it is worth mentioning the recent work [27], where the classical trajectory Monte Carlo (CTMC) method has been employed for calculations of FDCS. The scattered proton and emitted electron in this approach move along classical trajectories, and as compared to other aforementioned approaches, the CTMC method yields smaller disagreement between the calculations and experiment in terms of the binary-peak position. This provides a hint on how to cope with a problem clearly seen from previous works that the 3C function, having formally the proper radial asymptotics, apparently is unable to reproduce all the details of three-body final motion at large distances. Namely we can combine the 3C model with simple ideas of the quasiclassical postcollision interaction (PCI) approach [28]. We discuss this issue below in Sec. IV E.

Another important aspect to be pointed out with respect to the present study is that one can investigate various types of differential cross sections in the analysis of the COLTRIMS data. In particular, the following form of the fully differential cross section (FDCS) has been studied in Ref. [17]:

$$\text{FDCS} = \frac{d^5\sigma}{dE_e d\Omega_e d\Omega_p} = \frac{k_e m_p^2}{(2\pi)^5}|T_{fi}|^2, \tag{1}$$

where Ω_e and Ω_p specify the solid angles of the emitted electron and scattered proton, and T_{fi} is the scattering amplitude. In contrast, the work [16] plotted instead

$$\text{FDCS} = \frac{d^5\sigma}{dE_e d\theta_e d\phi_e dq d\phi_q} = |\sin\theta_e| \frac{k_e q}{(2\pi)^5 v_p^2}|T_{fi}|^2, \tag{2}$$

where θ_e and ϕ_e are the polar and azimuthal angles of the emitted electron relative to the beam axis, and ϕ_q is the azimuthal angle of the momentum transfer. Both FDCS forms, (1) and (2), carry a physically equivalent information about the ionizing collision. However, case (1) is customary for studying the binary and recoil peaks in the electron angular distribution and their shifts with respect to the FBA predictions. Case (2) is less convenient for such purposes, particularly when employing a logarithmic scale for the data representation, but appears to be informative about the effects which are hardly accessible for measurement and which we call "kinks." The latter features, which are also discussed in this work, owe to the asymmetry of the FDCS in the angular regions around the forward and backward directions determined by the proton velocity $\vec{v}_p$.

In our previous work we presented experimental data for the FDCS in the form (2). The experimental data from [16] and this work were obtained by definition together. However in this study we investigate a different kinematic regime. The wide spread of momentum transfer and electron energies presented herein provides further stringent tests for the theory. We also present a theoretical analysis in which we mainly address two issues. First, we examine the position of the experimental binary peak in comparison with FBA and 3C theories, particularly away from the Bethe ridge, which is specified by the energy- and momentum-transfer values equivalent to the projectile scattering on a free electron. Second, we examine the possible origin of disagreement between the 3C theory and experiment both in terms of collision dynamics in the internal and intermediate regions and in terms of asymptotic motion of final fragments in the outside

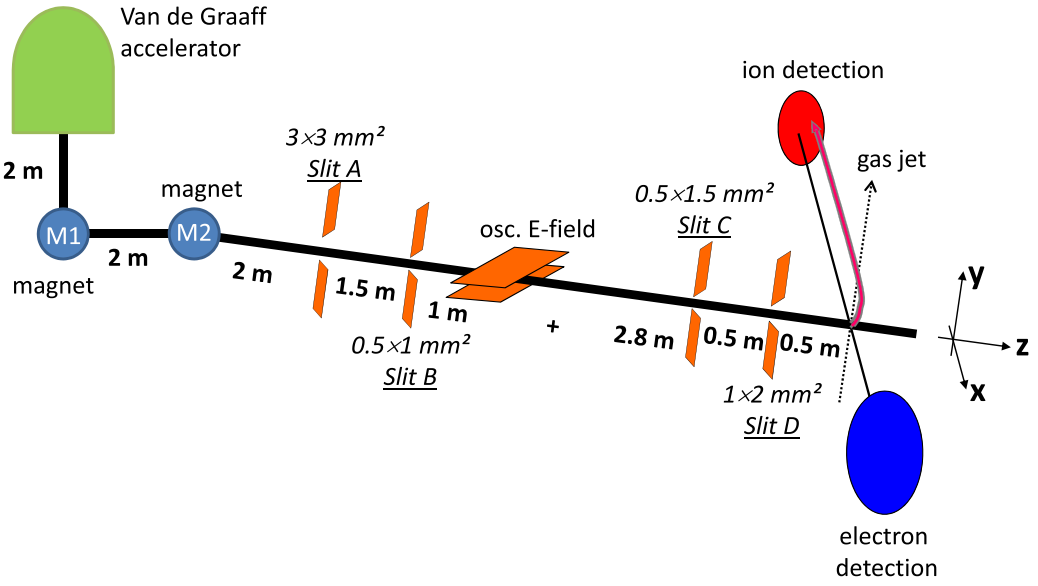

FIG. 1. Sketch of the beamline with its insertion devices. Bold printed numbers correspond to distances, while italic to slit opening ($x \times y$). Details are described in the text.

region. The paper is structured as follows. Section II describes details of experimental apparatus. In Sec. III, we formulate theoretical models and approximations for the considered process, which are involved in the present analysis. Then, in Sec. IV, we compare experimental and theoretical results. The conclusions are drawn in Sec. V. Atomic units (a.u.) in which $\hbar = e = m_e = 1$ are used throughout unless otherwise stated.

II. EXPERIMENT

The experiment was carried out at the Institut für Kernphysik at the University of Frankfurt using the 2.5-MeV Van de Graaf accelerator. The momentum vectors of the reaction fragments were measured using the well-established COLTRIMS technique [5]. A sketch of the beamline is shown in Fig. 1. The projectile beam of 1-MeV protons was first m/q and energy analyzed using a magnet (M1) at a deflection angle of 90°. About 2 m downstream a second magnet (M2) directs the beam in the corresponding experimental section (15°). 2 m downstream this second magnet, a first set of adjustable slits (A) with a rather large opening $3 \times 3\,\mathrm{mm}^2$ ($x \times y$), is placed. Another 1.5 m downstream another aperture (B) is placed, with an opening of $0.5 \times 1\,\mathrm{mm}^2$ ($x \times y$). Continuing, 3.8 m downstream, a third set of adjustable slits (C), with an opening of $0.5 \times 1.5\,\mathrm{mm}^2$, was placed, with the second and third defining the final beam geometry. To chop the beam and derive time-of-flight information, an oscillating electric field (≈150 V/cm) is applied on a 30-cm-long pair of deflector plates 1 m behind the first aperture (see [29]). The projectile buckets had a length of 1 ns (measured detecting charge exchange projectile ions) at a repetition rate of 2 MHz. Another fourth set of adjustable slits (D) is installed halfway between the third slit and the target and used to remove scattered projectiles, while not manipulating the main beam, so its opening was rather large compared to the third slit.

At a right angle, the projectile beam (along the z direction) is intersected with a precooled (40 K) supersonic helium gas jet (expanding in the y direction). With a driving pressure of 2 bars through a 30-μm nozzle, we estimated a speed ratio of >100, corresponding to an ion momentum resolution in this direction of $\Delta K_y < 0.1$ a.u. This geometry of the gas jet is defined by a set of skimmer and aperture, resulting in a jet diameter of 1.5 mm, a target density of 2×10^{11} atoms/cm^2, and a momentum resolution of <0.1 a.u. in the perpendicular directions (ΔK_x and ΔK_z). Electrons and ions, created in the intersection volume, are projected with a weak electric field of $E = 6.8$ V/cm towards two time- and position-sensitive detectors with hexagonal delay line anodes [30], with a diameter of 40 mm for the ion and 120 mm for the electron detection. Both the electron and ion arm of the spectrometer were built in a time-focusing geometry [31] to increase the momentum resolution along the time-of-flight axis (x). To further improve the momentum resolution for the ions, we additionally employed space focusing by adding an electrostatic lens in the acceleration region of the spectrometer (for details see Refs. [32–37]. In order to catch electrons up to 25 eV with a 4π solid angle, a weak magnetic field of 7.5 G was superimposed parallel to the electric field [38]. The momentum vectors of electron and He^+ ion are derived from the impact position on the corresponding detector, the particle's time of flight, the spectrometer geometry, and the strengths of electric and magnetic fields. As the projectile momentum is very difficult to measure directly, it was calculated with much higher total resolution from the measured electron and ion momenta by employing momentum conservation. As discussed in the Supplemental Material of [16], prior and after the experiment, calibration measurements for the ion arm of the spectrometer were performed, proofing a momentum resolution along the beam direction of $\Delta K_z = 0.1$ a.u. Based on the spectrometer and jet geometry, we estimated similar resolutions also for the x and y direction. For a detailed

discussion on how the analysis was performed, we refer to the Supplemental Material of [16].

III. THEORY

We begin with considering kinematical aspects of the discussed ionization reaction. From the momentum conservation law,

$$\vec{q} = \vec{k}_e + \vec{K}_{\rm ion}, \tag{3}$$

it follows that for the involved momentum-transfer and electron-energy values the velocity of the residual ion $K_{\rm ion}/(m_N+1)$ is practically negligible (the mass of the He atom is $m_N \approx 4m_p = 7344.6$ a.u.). This allows us to assume the ion to be at rest and choose the He nucleus as a center of the laboratory coordinate system. This assumption is valid for relatively small momentum-transfer values ($q \lesssim$ few a.u.).

The energy conservation law reads

$$\frac{p_i^2}{2m_p} + \varepsilon_0^{\rm He} = \frac{(\vec{p}_i - \vec{q})^2}{2m_p} + \varepsilon_0^{\rm He^+} + \frac{k_e^2}{2} + \frac{K_{\rm ion}^2}{2(m_N+1)}. \tag{4}$$

The terms $q^2/2m_p$ and $K_{\rm ion}^2/2(m_N+1)$ can be neglected in Eq. (4), and thus it reduces to the following equation:

$$v_p q_z = -\varepsilon_0^{\rm He} + \varepsilon_0^{\rm He^+} + E_e \tag{5}$$

(as indicated above, the z axis is directed along the initial proton momentum $\vec{p}_i$). The transverse component is $q_\perp \approx m_p v_p \theta_p$, with the proton scattering angle θ_p. For a given v_p value, the values of q and E_e are not arbitrary, being restricted by

$$\frac{0.9 + E_e}{q v_p} \leqslant 1. \tag{6}$$

Taking into account that $qdq = -p_i p_s d\cos\theta_p \approx m_p^2 v_p^2 \sin\theta_p d\theta_p$ and $d\phi_p = d\phi_q$, one obtains from Eq. (1) the FDCS in the form (2), which is studied in this work.

Let us turn to the issues related to evaluation of the scattering amplitude T_{fi}. The details of the FBA and 3C approaches were presented elsewhere [17]. Here we only give a diagrammatic representation of the amplitude using the 3C model. Figure 2 shows the basic diagrams for the 3C matrix element calculated in Ref. [17] (the rules for calculating the matrix elements on the basis of nonrelativistic diagrams are given, in particular, in Refs. [39–41]). The same as in Ref. [17], three initial trial helium wave functions Φ_i are employed in the present calculations: (i) a weakly correlated Roothaan-Hartree-Fock (RHF) [42] function, $\varepsilon_0^{\rm He} = -2.8617$ a.u., (ii) a simple Silverman-Platas-Matsen (SPM) function [43] of the configuration interaction family, $\varepsilon_0^{\rm He} = -2.8952$ a.u., and a strongly correlated function (CF) [44] which explicitly depends on the r_{12} distance between electrons in helium, $\varepsilon_0^{\rm He} = -2.9037$ a.u. The latter function yields the He energy which is very close to the experimental value, $\varepsilon_0^{\rm He} = -2.903\,724$ a.u.

In our analysis we also examine off-shell effects replacing the potentials V_{ep} and V_{pN} in diagrams shown in Fig. 2 by respectively the off-shell pair T matrices t_{ep} and t_{pN}. In such a way we distort the intermediate plane waves because $VG = tG_0$, where G and G_0 are full and free three-body

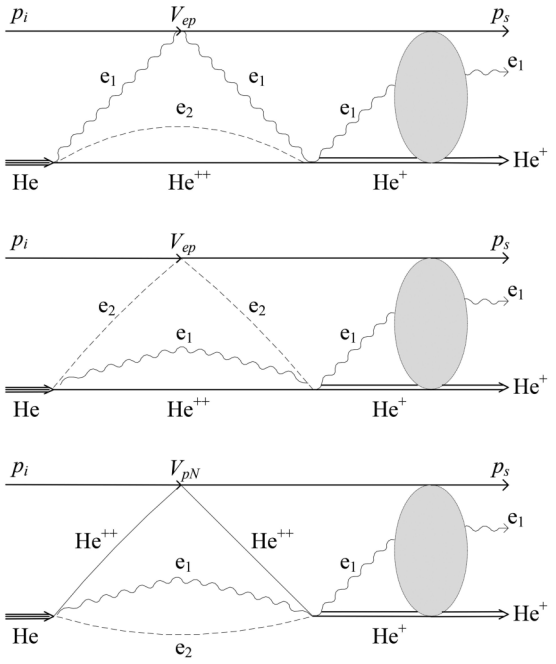

FIG. 2. Diagrammatic representation of the contributions A_1, A_2, and A_3 (from top to bottom) to the scattering amplitude calculated in Ref. [17] using the 3C model. The helium electrons are labeled with 1 and 2, and V_{ep} and V_{pN} are the electron-proton and proton-nucleus potentials, respectively.

Green's functions respectively. For the sake of simplicity, we analyze the indicated effect in the case of atomic hydrogen instead of the He atom. This also allows us to avoid the theoretical uncertainty associated with the He ground-state wave function. The corresponding diagrams are presented in Fig. 3.

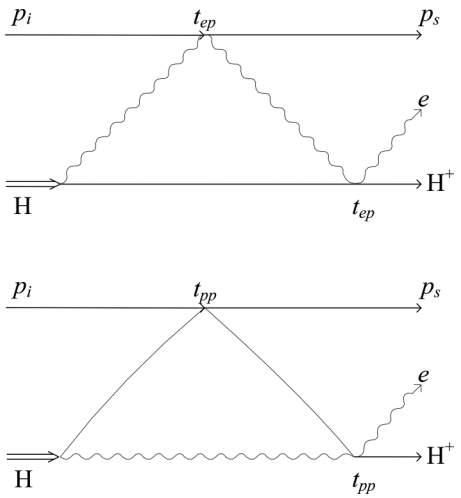

FIG. 3. Diagrammatic representation of the T_{ep} (top) and T_{pp} (bottom) components of the scattering amplitude for the ionization reaction $p + {\rm H} \to p + p + e$ when the pair potentials are replaced with the pair T matrices.

For the scattering amplitude we have the following mathematical expression:

$$T_{fi} = T_{ep} + T_{pp} = \int \frac{d^3g}{(2\pi)^3}\,\varphi_0(\vec{g})\,t_{ep}\left(\vec{v}_p - \vec{g}, \vec{v}_p - \vec{g} - \vec{q}; \frac{v_p^2}{2} + \varepsilon_0 - \vec{v}_p\cdot\vec{g}\right)\varphi^{-*}(\vec{g}+\vec{q}, \vec{k}_e)$$
$$+ \int \frac{d^3g}{(2\pi)^3}\,\varphi_0(\vec{g})\,t_{pp}\left(\frac{1}{2}(\vec{p}_i - \vec{g}), \frac{1}{2}(\vec{p}_i - \vec{g}) - \vec{q}; \frac{p_i^2}{4m} + \varepsilon_0 - \frac{1}{2}\,\vec{v}_p\cdot\vec{g} - \frac{g^2}{2}\right)\varphi^{-*}(\vec{g}, \vec{k}_e), \tag{7}$$

where

$$\varphi_0(\vec{g}) = \frac{8\sqrt{\pi}}{(1+g^2)^2}, \qquad \varepsilon_0 = -0.5,$$

and the Coulomb continuum function in momentum space is given by

$$\varphi^{-*}(\vec{p}, \vec{k}) = \lim_{\lambda\to+0}\left(-\frac{\partial}{\partial\lambda}\right)\int \frac{d^3r}{r}e^{-\lambda r}\tilde{\phi}^{-*}(\vec{r}, \vec{k})e^{i\vec{p}\cdot\vec{r}}$$
$$= \lim_{\lambda\to+0}\,4\pi\; e^{-\pi\zeta/2}\Gamma(1+i\zeta)\left(-\frac{\partial}{\partial\lambda}\right)\frac{[p^2 - (k+i\lambda)^2]^{i\zeta}}{[(\vec{p}-\vec{k})^2 + \lambda^2]^{(1+i\zeta)}}, \tag{8}$$

with the Sommerfeld parameter $\zeta = -1/k$. The Coulomb off-shell pair amplitudes t_{ep} and t_{pp} have the analytical representation (see, for example, Ref. [45])

$$t_{\alpha\beta}(\vec{p}, \vec{k}; E) = \lim_{\lambda\to+0}\frac{4\pi Z_\alpha Z_\beta}{q^2}\left[1 - 4i\eta_{\alpha\beta}\int_0^1 dy\,\frac{y^{i\eta_{\alpha\beta}}}{4y - \delta(1-y)^2 + i\lambda}\right]$$
$$= \frac{4\pi Z_\alpha Z_\beta}{q^2}\left\{1 + \frac{4i\eta_{\alpha\beta}}{\delta(1+i\eta_{\alpha\beta})(f_+ - f_-)}[x_+\,{}_2F_1(1,1;2+i\eta_{\alpha\beta};x_+) - x_-\,{}_2F_1(1,1;2+i\eta_{\alpha\beta};x_-)]\right\}, \tag{9}$$

where $q^2 = (\vec{p} - \vec{k})^2$,

$$\eta_{\alpha\beta} = \frac{Z_\alpha Z_\beta \mu_{\alpha\beta}}{\sqrt{2\mu_{\alpha\beta}E + i0}}, \quad \mu_{\alpha\beta} = \frac{m_\alpha m_\beta}{m_\alpha + m_\beta},$$

$$x_\pm = \frac{1}{1 - f_\pm},$$

$$\delta = 2\mu_{\alpha\beta}\frac{(E - p^2/2\mu_{\alpha\beta} + i0)(E - k^2/2\mu_{\alpha\beta} + i0)}{q^2(E + i0)},$$

$$f_\pm = 1 + \frac{2}{\delta}[1 \pm \sqrt{1+\delta}].$$

For the ep pair one has $Z_eZ_p = -1$, $\mu_{ep} \approx 1$, and

$$i\eta_{ep}(\vec{g}) = -\frac{i}{\sqrt{v_p^2 + 2\varepsilon_0^{\rm H} - 2\vec{v}_p\cdot\vec{g}}},$$

$$2E = \left(v_p^2 + 2\varepsilon_0^{\rm H} - 2\vec{v}_p\cdot\vec{g}\right) > 0, \tag{10}$$

$$i\eta_{ep}(\vec{g}) = -\frac{1}{\sqrt{\left|v_p^2 + 2\varepsilon_0^{\rm H} - 2\vec{v}_p\cdot\vec{g}\right|}},$$

$$2E = \left(v_p^2 + 2\varepsilon_0^{\rm H} - 2\vec{v}_p\cdot\vec{g}\right) < 0. \tag{11}$$

For the pp pair: $Z_pZ_p = 1$, $\mu_{pp} = m_p/2$, and $\eta_{pp} = 1/v_p$.

It should be noted that the FBA scattering amplitude is given by

$$T_{fi}^{\rm FBA}(\vec{q}, \vec{k}_e) = -\frac{4\pi}{q^2}\int \frac{d^3g}{(2\pi)^3}\,\varphi_0(\vec{g})\,\varphi^{-*}(\vec{g}+\vec{q}, \vec{k}_e)$$
$$= -\frac{(4\pi)^2}{\sqrt{\pi}\,q^2}\,e^{-\pi\zeta_e/2}\Gamma(1+i\zeta_e)\left(-\frac{\partial}{\partial\lambda}\right)_{\lambda=1}$$
$$\times\frac{[q^2 - (k_e+i\lambda)^2]^{i\zeta_e}}{[(\vec{q}-\vec{k}_e)^2 + \lambda^2]^{1+i\zeta_e}}. \tag{12}$$

In the limit of large v_p values one obtains

$$T_{pp} \approx \lim_{\lambda\to+0}\frac{4\pi}{q^2}|\Gamma(1+i/v_p)|^2\,e^{-(2i/v_p)\ln(v_pq)}\int\frac{d^3g}{(2\pi)^3}\,\varphi_0(\vec{g})$$
$$\times\left[\left(-\varepsilon_0 + \frac{1}{2}g^2\right)\left(\frac{1}{2}k_e^2 - \frac{1}{2}g^2 + i\lambda\right)\right]^{i/v_p}\varphi^{-*}(\vec{g}, \vec{k}_e), \tag{13}$$

$$T_{ep} \approx -\lim_{\lambda\to+0}\frac{4\pi}{q^2}|\Gamma(1+i/v_p)|^2\,e^{(2i/v_p)\ln(v_pq)}\int\frac{d^3g}{(2\pi)^3}\,\varphi_0(\vec{g})$$
$$\times\left[\left(-\varepsilon_0 + \frac{1}{2}g^2\right)\left(\frac{1}{2}k_e^2 - \frac{1}{2}(\vec{g}+\vec{q})^2 + i\lambda\right)\right]^{-i/v_p}$$
$$\times\,\varphi^{-*}(\vec{g}+\vec{q}, \vec{k}_e). \tag{14}$$

If in the integrand of Eq. (13) one sets $[\ldots]^{i/v_p} = 1$, then $T_{pp} = 0$. Note that we neglect the exchange proton-proton amplitude due to a very large difference between the proton velocities.

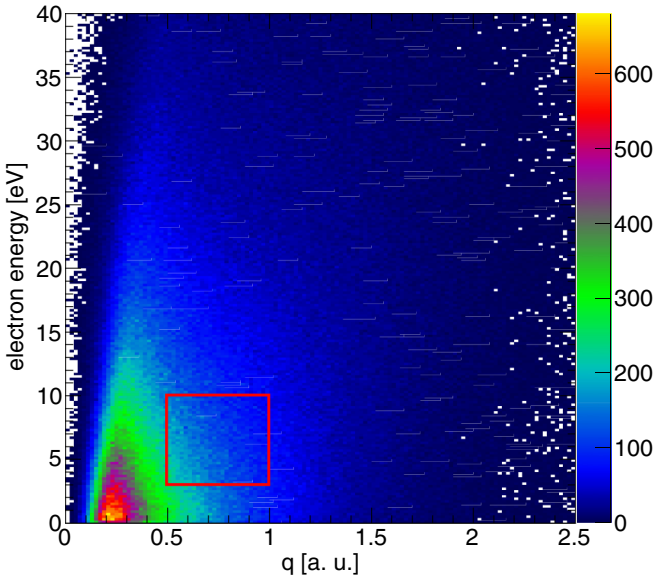

FIG. 4. Ionization events as a function of momentum transfer q and electron's kinetic energy E_e. The red box marks the kinematic conditions, chosen by Schulz *et al.* [46].

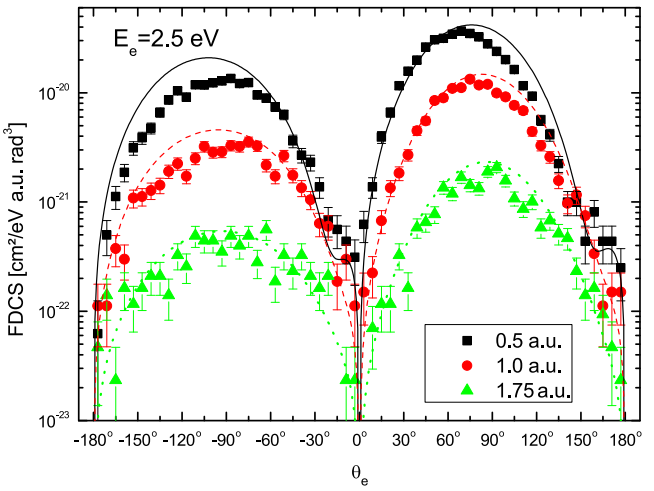

FIG. 5. Experimental angular distribution in the scattering plane for $E_e = 2.5 \pm 1$ eV kinetic energy. The black squares correspond to a momentum transfer $q = 0.5 \pm 0.15$ a.u., the red circles to $q = 1.0 \pm 0.25$ a.u., and the blue triangles to $q = 1.75 \pm 0.4$ a.u. The lines correspond to the model FBA + RHF (see details in the text) when $q = 0.5 \pm 0.15$ a.u. (solid black), $q = 1.0 \pm 0.25$ a.u. (dashed red), and $q = 1.75 \pm 0.4$ a.u. (dotted blue).

IV. RESULTS AND DISCUSSION

In this section we present the experimental data and numerical calculations for the FDCS in the form (2) at momentum-transfer values $q = 0.5$, 1.0, and 1.75 a.u. and (for each momentum-transfer value) the ejected-electron energies $E_e =$ 2.5, 5, 10, and 20 eV. To give an overview, the amount of events found in a certain kinematic region of momentum transfer q and electron energy E_e are shown in Fig. 4. Note that for $E_e > 25$ eV the solid angle decreases (first due to nodes caused by the gyration in the magnetic field and above 40 eV due to the limited overall size), as well as for $q > 2$ a.u. The red box marks the kinematic conditions originally chosen by Schulz *et al.* [46] and also used for the comparison with our calculations. However this box, respectively the events therein, does not coincide with the maximum of the ionization probability, which is exponentially decaying for E_e from 0 eV and having a maximum in the momentum transfer at $q =$ 0.22 a.u. Below we present results of numerical calculations for FDCS as a function of the electron scattering angle θ_e in the coplanar geometry, which were obtained using the theoretical approaches outlined in the previous section, and compare them with the experimental results.

A. Electron angular distribution: Experiment vs FBA

The FDCS measured in the scattering plane are shown in Figs. 5–8 along with the FBA calculations using the RHF model of the He ground state. In the calculations, the final state of the He atomic target (i.e., the $He^+ + e$ system) is orthogonalized to the RHF function. Moreover, we averaged the calculations within the experimental E_e and q gates: $E_e = 1.5$–3.5 eV (named $E_e = 2.5$ eV); $E_e = 3$–7 eV (named $E_e = 5$ eV); $E_e = 7.5$–12.5 eV (named $E_e = 10$ eV); $E_e = 15$–25 eV (named $E_e = 20$ eV); $q = 0.35$–0.65 (named $q = 0.5$); $q = 0.75$–1.25 (named $q = 1.0$); $q = 1.35$–2.15 (named $q = 1.75$). The experiment is normalized to the theory as follows: We selected the window $E_e < 25$ eV and $q < 2$ a.u., where we definitely have an electron solid-angle acceptance of 4π. The total number of counts within the selected window is 934 802, and the FBA integral cross section for this window is $\sigma(E_e < 25\text{ eV}, q < 2\text{ a.u.}) = 1.22 \times 10^{-17}$ cm^2. This gives a normalization factor of 13.06×10^{-24} cm^2/count. It should be noted that the value of the FBA total cross section, 2.21×10^{-17} cm^2, agrees well with the accepted value, 2.18×10^{-17} cm^2, from Ref. [47].

Some important comments should be made with regard to the results presented in Figs. 5–8. The origin of the kinks in the vicinity of $\theta_e = 0°, 180°$ lies in the FDCS definition (2), in which one has nodes at 0 and 180°, and the fact that the nodes of the physical electron angular distribution do

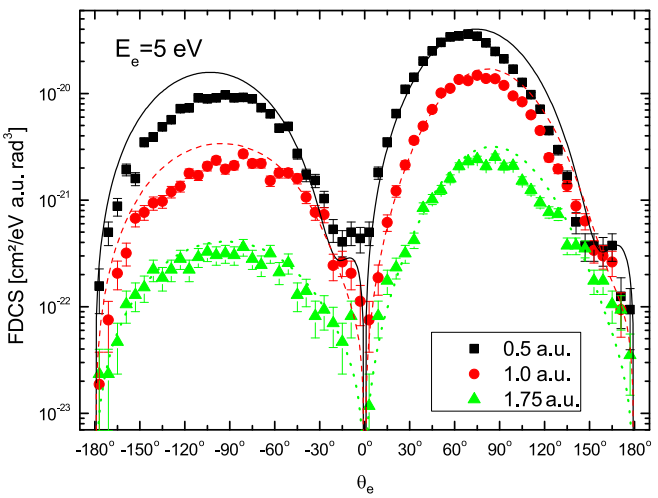

FIG. 6. The same as in Fig. 5, but for $E_e = 5 \pm 2$ eV.

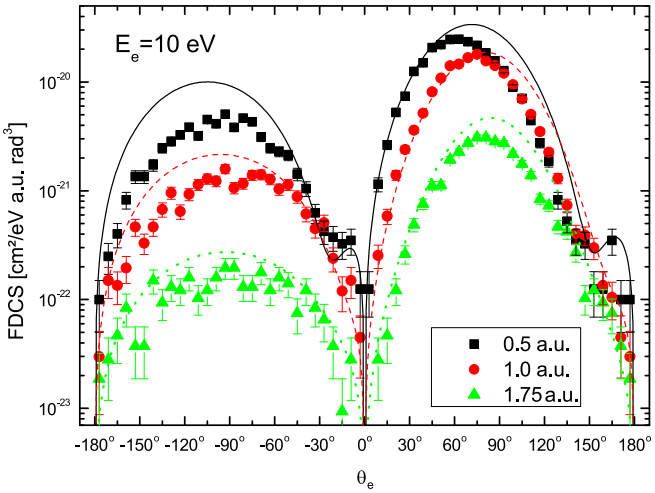

FIG. 7. The same as in Fig. 5, but for $E_e = 10 \pm 2.5$ eV.

not coincide with 0 and 180°. Further, in the angular region of the binary peak, the effects of convolution are practically not manifested. In particular, the shifts of the position of the theoretical binary peak due to the convolution are small. Let us note that a shift of the binary peak with respect to the FBA calculations was already observed and discussed in Ref. [16] (see also Refs. [22,27,48]). Therefore, we briefly outline the influence of convolution of theoretical values with experimental resolution and the integration over acceptance angles. In Ref. [16], the experimental data were integrated over a certain range of the perpendicular angles ($-10° < \phi_e < +10°$), electron energies ($3.0 < E_e < 10$ eV), and momentum transfers ($0.5 < q < 1.0$ a.u.), while the calculations were integrated only over ϕ_e. In Fig. 9 the electron angular distribution in the scattering plane is shown for the nonintegrated (red) and the integrated (black) calculation, according to the intervals chosen in the experiment. As can be seen from Figs. 5–8 the different electron energies (even in the integrated case) cause a systematic shift of the binary peak and an even stronger shift originates from different momentum transfers q. One might be misled to expect that symmetrically chosen experimental

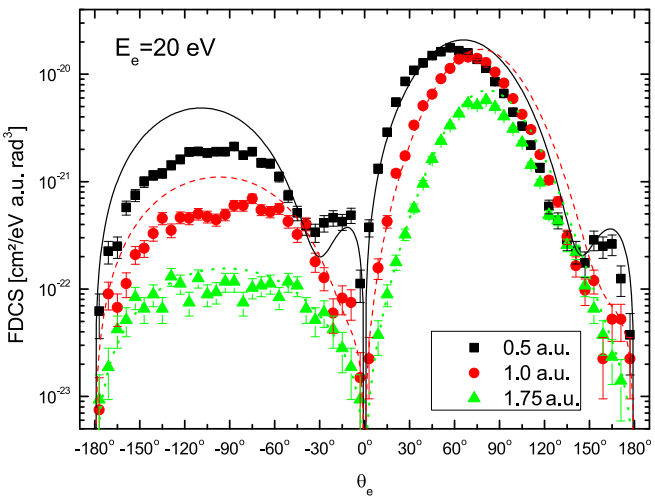

FIG. 8. The same as in Fig. 5, but for $E_e = 20 \pm 5$ eV.

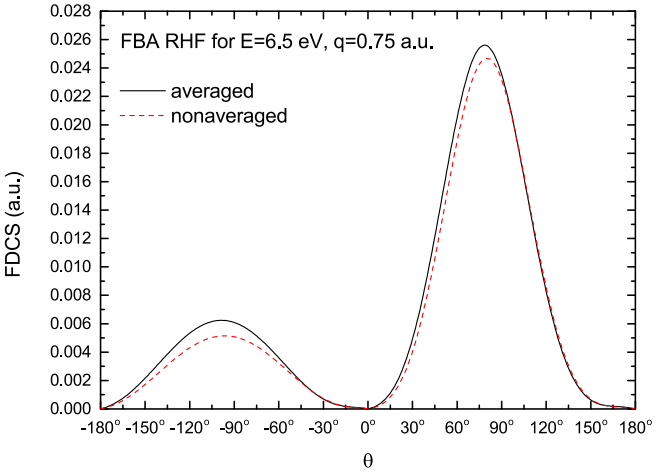

FIG. 9. The lines correspond to calculations in the FBA for a fixed momentum transfer $q = 0.75 \pm 0.25$ a.u. and electron energy $E_e = 6.5 \pm 3.5$ eV, as chosen in Ref. [16]. The dashed red curve shows the electron angular distribution for the nonintegrated data, i.e., fixed values, while the solid black curve takes the experimental boundary conditions properly into account, by integration over E_e and q within the indicated boundaries.

conditions would cancel out after integration over all electron energies and momentum transfers. Due to the fact that lower electron energies and momentum transfers contribute more to the total cross section than the larger values, a shift of $\approx 2°$ remains compared to the fixed values, as it is shown in Fig. 9.

The FBA theory is generally believed to be applicable if $|Z_p|/v_p \ll 1$ a.u., where Z_p and v_p are the charge and velocity of a fast ionic projectile. A very useful concept in the description of ionizing ion-atom collisions within the FBA is the Bethe surface, which represents the density of generalized oscillator strengths of an atomic target as a function of energy and momentum transfers (see, for instance, Ref. [49] and references therein). A marked feature of the Bethe surface common to all atomic systems is the Bethe ridge, which peaks when the energy and momentum transfers correspond to the kinematic regime of a free ion-electron collision and can be clearly identified at large momentum-transfer values. The Bethe ridge thus determines the phase-space region where the FBA mechanism gives largest contributions to the ionization yield, while far from this region one might expect other, more delicate mechanisms to come into play. In this context, it is interesting to point out that in terms of the peaks' positions the better agreement between theory and experiment in Figs. 5–8 is observed when the kinematic regime is closer to the Bethe ridge [49],

$$\frac{q^2}{2} = -\varepsilon_0^{\mathrm{He}} + \varepsilon_0^{\mathrm{He}^+} + E_e, \tag{15}$$

or, in accordance with Eq. (5), $q^2/2 = v_p q_z$. Note that the largest departure from the Bethe-ridge condition (15) is in the case of $q = 0.5$ a.u. and $E_e = 20$ eV. Therefore, in what follows, we focus on the shift of the binary peak in the indicated kinematic regime and on possible mechanisms underlying this shift.

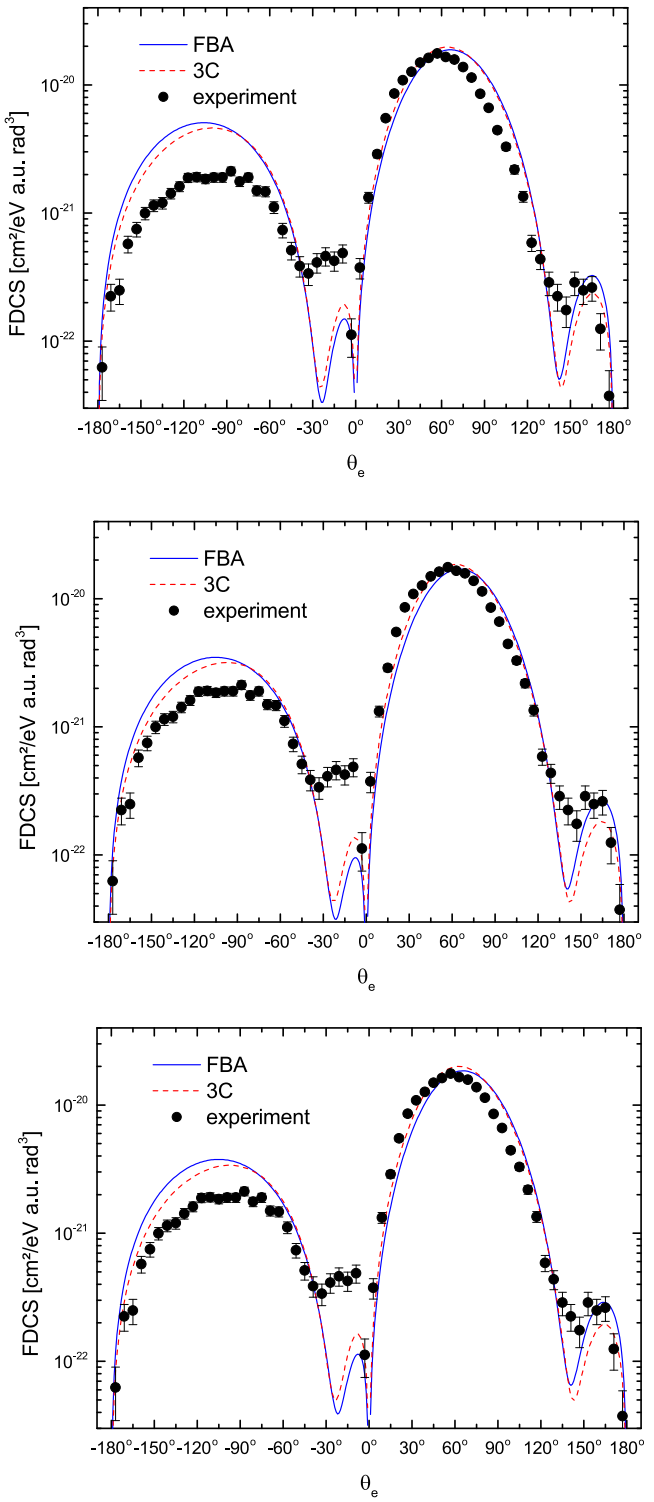

FIG. 10. FDCS in the scattering plane for $E_e = 20\,\text{eV}$, $q = 0.5$ a.u. The black squares represent the experiment, and the dashed red and solid blue lines represent respectively the 3C and FBA calculations using the RHF (top), SPM (middle), and CF (bottom) functions of He.

B. 3C model

In Fig. 10 the experimental data for $q = 0.5$ a.u. and $E_e = 20\,\text{eV}$ is compared to the unconvoluted FBA and 3C calculations using different functions of He. All differences, including the use of orthogonalization of the initial and final functions of helium, manifest themselves mainly in the vicinity of $\theta_e = 0°, 180°$, where the intensity is two orders of magnitude smaller than the peak intensity. Thus, the region of kinks appears to be most sensitive not only to the choice of a theoretical model, but also to the convolution of theory with experimental uncertainties (cf. Fig. 8, where convoluted FBA calculations are presented).

An analysis of the binary peak positions in the discussed kinematic regime shows that $\theta_{\text{bp}}^{\text{FBA}} \approx 65°$–$66°$, $\theta_{\text{bp}}^{\text{3C}} \approx 62°$–$64°$, and $\theta_{\text{bp}}^{\text{Exp}} \approx 57°$. It should be noted that, first, the position of the FBA binary peak in the case of the cross section (2) does not coincide with the direction of the momentum transfer $\vec{q}$; second, the binary-peak positions for different initial correlated functions of the He atom are very close to each other, and the shift mainly owes to the final 3C function. It is also worth noting that the discrepancy between the 3C theory and experiment in terms of the binary-peak position is about 5°–7°. From the viewpoint of the theory with a correlated final state, there are three ways to obtain a notable shift of the peak at high proton energy. Below we examine them separately.

C. Effective charges

In the calculations of the matrix elements diagrammatically shown in Fig. 2, the 3C function includes asymptotic values of charges of final fragments, i.e., $Z_e = -1$, $Z_p = +1$, $Z_{\text{He}^+} = +1$. In our previous study [17] we investigated the cases of switching off different pair interactions in the 3C function (see Fig. 5 of Ref. [17]). When we turned off the *pe* interaction, the binary peak shifted toward the proton direction, which was also observed by other authors. However, when we turned off the *pN* interaction, contrary to expectations, the binary peak shifted away from the proton direction. This effect seems to be counterintuitive and may indicate that the 3C function misses particular dynamical mechanisms in the asymptotic region, while describing more or less properly some intermediate reaction region outside the region of the direct knock-out collision inside the atom. In this intermediate region, apparently, the outgoing particle currents are formed, which in the outside, asymptotic region can be described within the PCI framework. In such a case, one can "play" with the Sommerfeld parameters of the 3C function by varying the involved particle charges. We find that if, for example, the contribution of the *pN* interaction is increased due to increasing the effective charge of the He^+ ion, while the contribution of the *pe* interaction is decreased, then in the kinematic regime under consideration, $E_e = 20\,\text{eV}$ and $q = 0.5$ a.u., one can shift the binary peak as much as almost to agree with experiment, but at the same time the values of the effective charges appear to be manifestly unrealistic. Clearly, such an approach is rather mechanistic and lacks physical justification.

D. Effects of pair *T* matrices

Figure 11 shows the numerical results for the $p + \text{H} \to p + p + e$ process in the following kinematic regime: $E_p = 1\,\text{MeV}$, $E_e = 20\,\text{eV}$, and $q = 0.5$ a.u. The results are obtained on the basis of Eqs. (7)–(14), and the details of

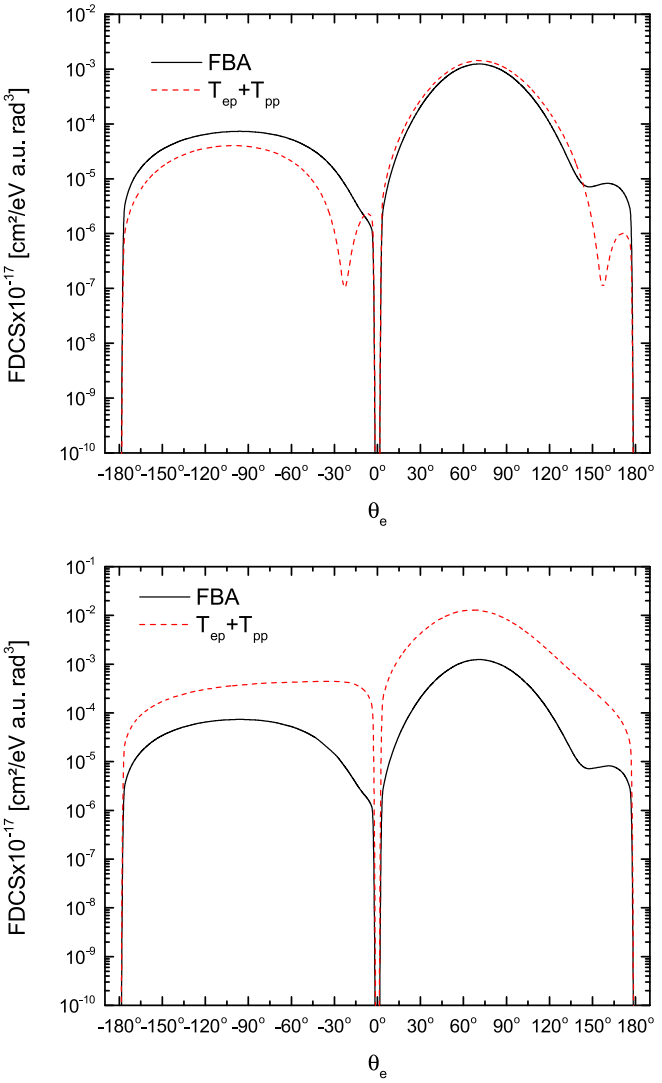

FIG. 11. FDCS in the scattering plane for the $p + \mathrm{H} \to p + p + e$ reaction at $E_p = 1\,\mathrm{MeV}$, $E_e = 20\,\mathrm{eV}$, and $q = 0.5$ a.u. Top: results of calculations based on Eqs. (13) and (14). Bottom: results of calculations based on Eqs. (9) and (10) for t_{ep} in Eq. (7) and Eq. (13) for T_{pp}.

a numerical scheme employed for calculating the involved integrals can be found in Ref. [50]. As pointed out in Sec. III, using in the analysis the atomic hydrogen target instead of helium not only simplifies the calculations but also helps to avoid the theoretical uncertainty related to the ground-state He wave function. In the top panel of Fig. 11, one can see well-pronounced kinks, as well as almost complete agreement with FBA in the peak region, which is expected at high proton energies. There is no shift of the binary peak in comparison with FBA. In the bottom panel of Fig. 11 there are no kinks, and there is a significant difference compared to FBA. This owes to the contribution from large values of intermediate electron momenta g to the integral T_{ep} in Eq. (7). However, there is still no shift of the binary peak. We also note that the calculations showed insignificance of the contribution from the bound-state energy region (11) to the T_{ep} amplitude. Thus, the replacement of the pair potentials by the pair T matrices

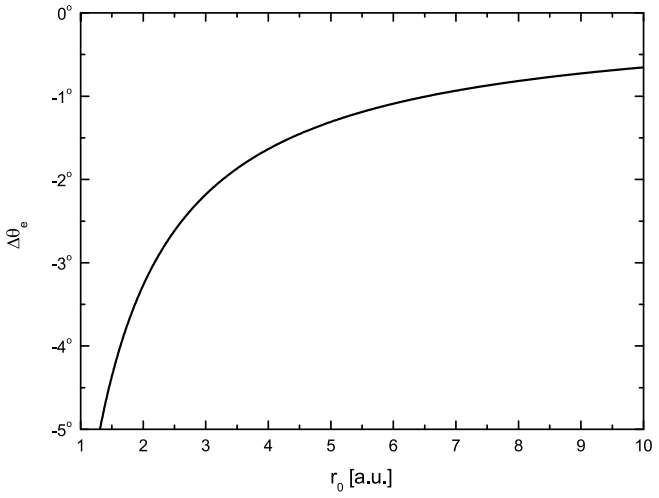

FIG. 12. The numerical estimate of the shift of the binary peak in accordance with Eq. (16).

can hardly stand behind the mechanism responsible for the shifting of a binary peak in the He case.

E. PCI effects

In Ref. [28], a general formula was obtained for the deflection of charged particles, which after being emitted from the quantum three-particle interaction region restricted by a finite radius r_0 continue to move along classical trajectories before hitting the detectors. Obviously, these trajectories for charged particles are not straight lines, and if on the boundary of the region the cross section could be represented in the form $\mathrm{FDCS}(\theta_p, \theta_e)$, then the measured cross section will be $\mathrm{FDCS}(\theta_p + \Delta\theta_p, \theta_e + \Delta\theta_e)$. The formula was obtained for the case when both the scattered projectile and the ejected electron are relatively fast, but for estimations it can also be applied to an ionized electron with an energy of as low as 20 eV (see below). From Ref. [28] it follows that

$$\Delta\theta_\alpha = \frac{Z_p Z_e}{E_\alpha r_0} \times \frac{v_\alpha \cos(\chi_0/2)[|\vec{v}_p - \vec{v}_e| + 2v_\beta \sin(\chi_0/2)]}{4|\vec{v}_p - \vec{v}_e| \sin(\chi_0/2)[|\vec{v}_p - \vec{v}_e| + (v_p + v_e)\sin(\chi_0/2)]},$$
$$\chi_0 = \theta_e + \theta_p. \tag{16}$$

Due to the huge energy of the final proton ($\alpha = p$, $\beta = e$), its deflection can be neglected. At the same time, by varying the r_0 value, one can get the required shift of the binary peak from clear physical principles. It should be kept in mind that the cross section $\mathrm{FDCS}(\theta_p, \theta_e)$ is formed within the 3C model inside the region bounded by the radius r_0, which in turn can depend on q and E_e. Figure 12 shows the dependence of the angular shift $\Delta\theta_e$ of the binary peak ($\theta_{\max}^{CF} \approx 63^\circ$) on the parameter r_0 for the kinematic regime $q = 0.5$ a.u. and $E_e = 20\,\mathrm{eV}$. It turns out that the semiclassical PCI model can more or less explain the shift of the binary peak. However, we should consider the 3C function as having the effect in the intermediate region which separates the region of the direct pe collision from that of the asymptotic motion of outgoing particles.

V. SUMMARY AND CONCLUSIONS

We have studied experimental fully differential cross sections for single ionization of the He atom by a fast proton with an energy of 1 MeV in comparison with various theoretical approaches. The results of the FBA model have been integrated over experimental acceptance intervals. The change in the agreement between theory and experiment with varying the energy of the ejected electron E_e and the momentum transfer q has been shown. We have observed worse agreement between the FBA theories and experiment for E_e and q values away from the Bethe ridge. We have investigated into the physical mechanism which could explain the large discrepancy between the positions of the theoretical and experimental binary peaks when $E_e = 20\,\text{eV}$ and $q = 0.5\,\text{a.u.}$, i.e., when the kinematic departure from the Bethe ridge is maximal. The convolution of the theory with experimental uncertainties has been found to be insufficient for explaining the indicated discrepancy. Taking into account the electron correlations in the ground He state and employing the 3C model for the final scattering state are also not sufficient. Finally, various other customary approaches beyond the FBA and 3C models have been considered. The method of effective charges has been found not to shift the binary peak within realistic physical assumptions. Replacing potentials by pair T matrices, when one takes into account the off-shell effects, also has been found to be insufficient. Only the semiclassical PCI effect can in principle yield agreement with experiment provided this effect is combined with the 3C model. However, in this particular case we have to suppose that the 3C function does not describe properly all the asymptotic effects for the three-particle motion in the final state. Thus, our analysis clearly shows the limitations of the FBA-like theories even at impact energies as high as 1 MeV when one is far from the Bethe-ridge regime.

ACKNOWLEDGMENTS

The present research benefited from computational resources made available on the supercomputer Lomonosov from Moscow State University, Central Information and Computer Complex of the Joint Institute for Nuclear Research, and HybriLIT heterogeneous computing cluster. Y.P. is grateful to Russian Foundation for Basic Research (RFBR) for the financial support under Grant No. 19-02-00014-a. O.C. acknowledges support from the Hulubei-Meshcheryakov program JINR-Romania. M.S. acknowledges financial support from the Deutsche Forschungsgemeinschaft (DFG).

[1] G. S. Was, *Fundamentals of Radiation Materials Science* (Springer-Verlag, New York, 2017).

[2] *Ion Beam Therapy*, edited by U. Linz (Springer-Verlag, Berlin, Heidelberg, 2012).

[3] H.-K. Kim, J. Titze, M. Schöffler, F. Trinter, M. Waitz, J. Voigtsberger, H. Sann, M. Meckel, C. Stuck, U. Lenz, D. Metz, A. Jung, M. Odenweller, N. Neumann, S. Schössler, K. Ullmann-Pfleger, B. Ulrich, R. Costa Fraga, N. Petridis, D. Metz *et al.*, Proc. Natl. Acad. Sci. USA **108**, 11821 (2011).

[4] J. Ullrich, R. Moshammer, R. Dörner, O. Jagutzki, V. Mergel, H. Schmidt-Böcking, and L. Spielberger, J. Phys. B **30**, 2917 (1997).

[5] R. Dörner, V. Mergel, O. Jagutzki, L. Spielberger, J. Ullrich, R. Moshammer, and H. Schmidt-Böcking, Phys. Rep. **330**, 95 (2000).

[6] J. Ullrich, R. Moshammer, A. Dorn, R. Dörner, L. Ph. H. Schmidt, and H. Schmidt-Böcking, Rep. Prog. Phys. **66**, 1463 (2003).

[7] D. Misra, H. T. Schmidt, M. Gudmundsson, D. Fischer, N. Haag, H. A. B. Johansson, A. Källberg, B. Najjari, P. Reinhed, R. Schuch, M. Schöffler, A. Simonsson, A. B. Voitkiv, and H. Cederquist, Phys. Rev. Lett. **102**, 153201 (2009).

[8] J. Titze, M. S. Schöffler, H.-K. Kim, F. Trinter, M. Waitz, J. Voigtsberger, N. Neumann, B. Ulrich, K. Kreidi, R. Wallauer, M. Odenweller, T. Havermeier, S. Schössler, M. Meckel, L. Foucar, T. Jahnke, A. Czasch, L. Ph. H. Schmidt, O. Jagutzki, R. E. Grisenti *et al.*, Phys. Rev. Lett. **106**, 033201 (2011)

[9] L. Ph. H. Schmidt, T. Jahnke, A. Czasch, M. Schöffler, H. Schmidt-Böcking, and R. Dörner, Phys. Rev. Lett. **108**, 073202 (2012).

[10] M. Schulz, X. Wang, M. Gundmundsson, K. Schneider, A. Kelkar, A. B. Voitkiv, B. Najjari, M. Schöffler, L. Ph. H. Schmidt, R. Dörner, J. Ullrich, R. Moshammer, and D. Fischer, Phys. Rev. Lett. **108**, 043202 (2012).

[11] M. S. Schöffler, C. Stuck, M. Waitz, F. Trinter, T. Jahnke, U. Lenz, M. Jones, A. Belkacem, A. L. Landers, M. S. Pindzola, C. L. Cocke, J. Colgan, A. Kheifets, I. Bray, H. Schmidt-Böcking, R. Dörner, and T. Weber, Phys. Rev. Lett. **111**, 013003 (2013).

[12] H. R. Dodd and K. R. Greider, Phys. Rev. **146**, 675 (1966).

[13] R. Gayet, J. Phys. B: At. Mol. Phys. **5**, 483 (1972).

[14] M. S. Pindzola, J. Colgan, F. Robicheaux, T. G. Lee, M. F. Ciappina, M. Foster, J. A. Ludlow, and S. A. Abdel-Naby, Adv. At. Mol. Opt. Phys. **65**, 291 (2016).

[15] I. B. Abdurakhmanov, A. S. Kadyrov, I. Bray, and A. T. Stelbovics, J. Phys. B: At. Mol. Opt. Phys. **44**, 075204 (2011).

[16] H. Gassert, O. Chuluunbaatar, M. Waitz, F. Trinter, H.-K. Kim, T. Bauer, A. Laucke, C. Müller, J. Voigtsberger, M. Weller, J. Rist, M. Pitzer, S. Zeller, T. Jahnke, L. Ph. H. Schmidt, J. B. Williams, S. A. Zaytsev, A. A. Bulychev, K. A. Kouzakov, H. Schmidt-Böcking *et al.*, Phys. Rev. Lett. **116**, 073201 (2016).

[17] O. Chuluunbaatar, S. A. Zaytsev, K. A. Kouzakov, A. Galstyan, V. L. Shablov, and Y. V. Popov, Phys. Rev. A **96**, 042716 (2017).

[18] M. Brauner, J. S. Briggs, and H. Klar, J. Phys. B: At. Mol. Opt. Phys. **22**, 2265 (1989).

[19] D. Belkic, R. Gayet, and A. Salin, Phys. Rep. **56**, 279 (1979).

[20] D. S. F. Crothers and L. J. Dube, Adv. At. Mol. Opt. Phys. **30**, 287 (1993).

[21] I. Bray, Phys. Rev. A **49**, 1066 (1994).

[22] A. B. Voitkiv, Phys. Rev. A **95**, 032708 (2017).

[23] P. D. Fainstein and V. D. Rodriguez, J. Phys. B: At. Mol. Opt. Phys. **33**, 4637 (2000).

[24] I. B. Abdurakhmanov, A. S. Kadyrov, I. Bray, and A. T. Stelbovics, J. Phys. B: At. Mol. Opt. Phys. **44**, 165203 (2011).
[25] M. F. Ciappina, T.-G. Lee, M. S. Pindzola, and J. Colgan, Phys. Rev. A **88**, 042714 (2013).
[26] M. Schulz, B. Najjari, A. B. Voitkiv, K. Schneider, X. Wang, A. C. Laforge, R. Hubele, J. Goullon, N. Ferreira, A. Kelkar, M. Grieser, R. Moshammer, J. Ullrich, and D. Fischer, Phys. Rev. A **88**, 022704 (2013).
[27] L. B. Sarkadi, Phys. Rev. A **97**, 042703 (2018).
[28] Y. V. Popov and V. F. Erokhin, Phys. Lett. A **97**, 280 (1983)
[29] T. Weber, K. Khayyat, R. Dörner, V. Mergel, O. Jagutzki, L. Schmitt, F. Afaneh, A. Gonzales, C. L. Cocke, A. L. Landers, and H. Schmidt-Böcking, J. Phys. B: At. Mol. Opt. Phys. **33**, 3331 (2000).
[30] O. Jagutzki, A. Cerezo, A. Czasch, R. Dörner, M. Hattass, M. Huang, V. Mergel, U. Spillmann, K. Ullmann-Pfleger, T. Weber, H. Schmidt-Böcking, and G. D. W. Smith, IEEE Trans. Nucl. Sci. **49**, 2477 (2002).
[31] W. C. Wiley and I. H. McLaren, Rev. Sci. Instrum. **26**, 1150 (1955).
[32] R. Dörner, V. Mergel, L. Spielberger, M. Achler, K. Khayyat, T. Vogt, H. Bräuning, O. Jagutzki, T. Weber, J. Ullrich, R. Moshammer, M. Unverzagt, W. Schmitt, H. Khemliche, M. H. Prior, C. L. Cocke, J. Feagin, R. E. Olson, and H. Schmidt-Böcking, Nucl. Instrum. Methods Phys. Res., Sect. B **124**, 225 (1997).
[33] H.-K. Kim, M. S. Schöffler, S. Houamer, O. Chuluunbaatar, J. N. Titze, L. Ph. H. Schmidt, T. Jahnke, H. Schmidt-Böcking, A. Galstyan, Y. V. Popov, and R. Dörner, Phys. Rev. A **85**, 022707 (2012).
[34] M. S. Schöffler, J. N. Titze, L. Ph. H. Schmidt, T. Jahnke, O. Jagutzki, H. Schmidt-Böcking, and R. Dörner, Phys. Rev. A **80**, 042702 (2009).
[35] M. Schöffler, A. L. Godunov, C. T. Whelan, H. R. J. Walters, V. S. Schipakov, V. Mergel, R. Dörner, O. Jagutzki, L. Ph. H. Schmidt, J. Titze, E. Weigold, and H. Schmidt-Böcking, J. Phys. B **38**, L123 (2005).
[36] A. L. Godunov, C. T. Whelan, H. R. J. Walters, V. S. Schipakov, M. Schöffler, V. Mergel, R. Dörner, O. Jagutzki, L. Ph. H. Schmidt, J. Titze, and H. Schmidt-Böcking, Phys. Rev. A **71**, 052712 (2005).
[37] M. S. Schöffler, J. Titze, L. Ph. H. Schmidt, T. Jahnke, N. Neumann, O. Jagutzki, H. Schmidt-Böcking, R. Dörner, and I. Mancev, Phys. Rev. A **79**, 064701 (2009).
[38] R. Moshammer, M. Unverzagt, W. Schmitt, J. Ullrich, and H. Schmidt-Böcking, Nucl. Instrum. Methods Phys. Res., Sect. B **108**, 425 (1996).
[39] P. S. Vinitsky, Y. V. Popov, and O. Chuluunbaatar, Phys. Rev. A **71**, 012706 (2005).
[40] V. V. Komarov and A. M. Popova, Zh. Eksp. Teor. Fiz. **46**, 2112 (1964) [Sov. Phys. JETP **19**, 1425 (1964)].
[41] V. V. Komarov, S. G. Serebrjakov, and A. M. Popova, Phys. Lett. B **34**, 275 (1971).
[42] E. Clementi and C. Roetti, At. Data Nucl. Data Tables **14**, 177 (1974).
[43] J. N. Silvermann, O. Platas, and F. A. Matsen, J. Chem. Phys. **32**, 1402 (1960).
[44] O. Chuluunbaatar, I. V. Puzynin, P. S. Vinitsky, Y. V. Popov, K. A. Kouzakov, and C. Dal Cappello, Phys. Rev. A **74**, 014703 (2006).
[45] C. S. Shastry, L. Kumar, and J. Callaway, Phys. Rev. A **1**, 1137 (1970)
[46] M. Schulz, R. Moshammer, D. Fischer, H. Kollmus, D. H. Madison, S. Jones, and J. Ullrich, Nature (London) **422**, 48 (2003).
[47] C. F. Barnett, Oak Ridge National Laboratory, Report No. ORNL-6086, Vol. 1, 1990.
[48] I. B. Abdurakhmanov, A. S. Kadyrov, I. Bray, and K. Bartschat, Phys. Rev. A **96**, 022702 (2017).
[49] M. Inokuti, Rev. Mod. Phys. **43**, 297 (1971).
[50] O. Chuluunbaatar, K. Kouzakov, and Y. Popov, Eur. Phys. J.: Web Conf. **173**, 03007 (2018).